

**A rod-linear cascade model for emulating rotor-stator interaction noise in turbofans  
A numerical study**

Teruna, Christopher; Ragni, Daniele; Avallone, Francesco; Casalino, Damiano

**DOI**

[10.1016/j.ast.2019.04.047](https://doi.org/10.1016/j.ast.2019.04.047)

**Publication date**

2019

**Document Version**

Final published version

**Published in**

Aerospace Science and Technology

**Citation (APA)**

Teruna, C., Ragni, D., Avallone, F., & Casalino, D. (2019). A rod-linear cascade model for emulating rotor-stator interaction noise in turbofans: A numerical study. *Aerospace Science and Technology*, 90, 275-288. <https://doi.org/10.1016/j.ast.2019.04.047>

**Important note**

To cite this publication, please use the final published version (if applicable).  
Please check the document version above.

**Copyright**

Other than for strictly personal use, it is not permitted to download, forward or distribute the text or part of it, without the consent of the author(s) and/or copyright holder(s), unless the work is under an open content license such as Creative Commons.

**Takedown policy**

Please contact us and provide details if you believe this document breaches copyrights.  
We will remove access to the work immediately and investigate your claim.

***Green Open Access added to TU Delft Institutional Repository***

***'You share, we take care!' – Taverne project***

**<https://www.openaccess.nl/en/you-share-we-take-care>**

Otherwise as indicated in the copyright section: the publisher is the copyright holder of this work and the author uses the Dutch legislation to make this work public.



# A rod-linear cascade model for emulating rotor-stator interaction noise in turbofans: A numerical study

Christopher Teruna\*, Daniele Ragni, Francesco Avallone, Damiano Casalino

Delft University of Technology, Kluyverweg 1, Delft, the Netherlands

## ARTICLE INFO

### Article history:

Received 27 December 2018  
 Received in revised form 4 April 2019  
 Accepted 26 April 2019  
 Available online 2 May 2019

### Keywords:

Rod-airfoil  
 Rotor/stator interaction  
 Linear cascade  
 Turbulence impingement noise

## ABSTRACT

This manuscript presents a rod-linear cascade model for emulating rotor-stator interaction noise. The model is intended as a test platform for studying noise mitigation techniques for a turbofan fan stage, while it also extends the classical rod-airfoil configuration by considering a row of blades based on realistic geometrical details. The rod-linear cascade model consists of a rod positioned upstream of a 7-blade linear cascade, such that the rod wake impinges onto the central blade. The rod is scaled to obtain a fundamental shedding frequency equal to the first blade passing frequency of the NASA-Glenn Source Diagnostics Test (SDT) fan stage at *approach* condition. The cascade blade profile is also based on the OGV of the SDT sampled at 90% of the radial span. Subsequently, numerical simulations are performed using lattice-Boltzmann Method on a computational setup comprised of a contraction and a test section enclosing the rod-linear cascade model. The integral length scales of the rod wake and the mean loading of the central blade have been found to be in good agreement with the trends observed in the SDT fan stage. The primary noise sources are localized at the central blade leading edge, although noise propagation to the far-field is influenced by additional diffraction by the other blades. Furthermore, the acoustic-blade row interaction causes intense pressure fluctuation within the inter-blade channels, including in those that are not directly affected by the rod wake.

© 2019 Published by Elsevier Masson SAS.

## 1. Introduction

One of the noise generation mechanisms in an aeroengine is the rotor-stator interaction [1], which involves periodic impingement of the rotor wake on the stator. The process causes unsteady loading on the stator surface followed by noise radiation with both tonal and broadband components [2]. Rotor-stator interaction in a modern high-bypass turbofan can be found, for instance, in the fan stage, where the turbulent fan (rotor) wake interacts with the outlet guide vanes (OGV/stator). The interaction process is also expected to become more significant as future designs are heading towards higher bypass ratio [3], since the increased engine diameter would be accompanied with reduced axial length due to weight and structural constraints. This causes the fan wake to be more coherent when impinging the OGV, resulting in increased tonal noise production. Considering this trend, it is of practical interests to gain further insights on the aeroacoustics of the noise generation mechanism and to explore potential noise mitigation strategies. Nonetheless, investigating a complex system, such as a complete fan stage, may become quite challenging and expen-

sive, especially in early stages of design. Instead, it would be more feasible to first examine models based on simplified geometrical elements that still preserve the flow features of interest. A number of models have been proposed for studying various aviation noise sources, such as the tandem cylinder configuration for landing gear noise [4–6], the rod-airfoil configuration for blade-vortex interaction in helicopter and rotor-stator interaction in turbofan [7,8], and square cylinder-wedge configuration for high-lift devices noise [9].

The rod-airfoil configuration (RAC) has been quoted to be suitable for emulating the rotor-stator interaction mechanism due to the quasi-tonal and broadband excitation induced by the rod wake onto the airfoil [7,8,10–12]. The classical RAC consists of a rod positioned upstream of an airfoil, and it was introduced as a benchmark configuration for computational aeroacoustics (CAA) studies on turbulent wake-body interaction [7,13–16]. However, there are various features inherent of the rotor-stator aeroacoustics which are absent in the RAC due to the usage of the isolated, symmetrical airfoil; two among which will be addressed in this manuscript. Firstly, typical stator vanes in a fan stage are designed with large camber, installed at high incidence angle, and arranged in a cascade to achieve significant flow deflection. Secondly, the high-solidity environment typical of a fan stage results in significant acoustic interactions between one blade and its neighbors [17,18].

\* Corresponding author.

E-mail address: c.teruna@tudelft.nl (C. Teruna).

Collectively, these aerodynamics and aeroacoustics implications are often referred to as cascade effects.

To demonstrate the significance of cascade effects, Finez et al. [19] previously performed experimental measurement on the trailing edge noise of a linear cascade. They observed that Amiet's isolated airfoil model [20] underpredicted their measurements by 5–20 dB at low to mid frequency ranges. The authors obtained better results using the modified Glegg's cascade trailing edge noise model [17] with additional corrections to compensate for the imperfect periodicity of the experimental setup. They also discovered that the cascade effects are more prominent at frequency ranges where the acoustic wavelength is larger than the blade-to-blade separation.

Meanwhile, other studies have shown how geometrical details may influence the cascade acoustics response, particularly for the tonal noise component [21–25]. In a recent study, De Laborderie et al. have investigated the camber effects to cascade acoustics response [25]. They extended the flat-plate-cascade acoustic model of Posson et al. [26] by including the camber effects, and applied the model on a single-stage axial compressor. The results were also compared to CAA (Computational Aero-Acoustics) computations based on 3D compressible Navier-Stokes equations [27]. The inclusion of camber effects to the acoustic model was shown to improve the agreement of the analytical model against the CAA results.

Consequently, replacing the isolated airfoil of the RAC with a linear cascade is beneficial for obtaining a more representative setup for emulating the fan wake-OGV impingement mechanism, hence the rod-linear cascade model (RLC). The cascade profile and the forcing period of the rod wake are also derived from those of the NASA-Glenn Source Diagnostic Test (SDT) fan stage. However, the RLC only considers one blade that undergoes rod wake impingement for the following reasons: 1) it would be difficult to synchronize the phase of the vortex shedding from multiple rods to match the phase relation between the wake impingement on one blade and the others, as in the case of a real turbofan, and 2) to avoid unwanted feedback mechanism due to the presence of multiple vortex streets close to each other [28]. To this scope, this manuscript aims at characterizing the aerodynamics and aeroacoustics features of the rod-linear cascade model. The study is performed using commercial lattice-Boltzmann solver, PowerFLOW, to reproduce the RLC setup as closely as possible to an experimental setting. Moreover, the outlook of this study is to employ the RLC for studying the effects of various noise mitigation techniques in a turbomachinery-like flow field, including potential impacts on the aerodynamic performance.

This paper is organized as follows. Section 2 provides the description of the methodologies used in this paper, including a brief overview of lattice-Boltzmann method in PowerFLOW, the rod-linear cascade configuration, and details of the simulation setup. Section 3 discusses the computational results on the rod-linear cascade test rig, including a grid independence study. A summary of this paper is reported in section 4.

## 2. Methodology

### 2.1. Numerical technique

This section describes the numerical technique of the commercial solver SIMULIA PowerFLOW 5.4b, a solver based on lattice-Boltzmann Method (LBM). The same methodology has also been used previously for studying the RAC [14] and the tandem cylinder configuration [6]. Further details on the methodology can be found in [29].

The LBM is derived from the Boltzmann's kinetic theory of gases which describes the motion of fluid particles on microscopic

level, such as random movement (i.e., Brownian motion) and particle collision. These phenomena can be mathematically expressed as the Boltzmann transport equation (BTE), in which the states of each particle (e.g., position and momentum) are given as probability distribution functions. After neglecting the body forces, the BTE is mathematically expressed as follows.

$$\frac{\partial F}{\partial t} + \vec{V} \cdot \nabla F = \mathbf{C} \quad (1)$$

where  $F(\vec{x}, t)$  is the particle distribution function in spatial ( $\vec{x}$ ) and temporal dimension ( $t$ ),  $\vec{V}$  is the particle velocity vector, and  $\mathbf{C}$  is the collision operator. With the LBM approach, the BTE is discretized onto a Cartesian grid (i.e., lattice) where fluid particles are confined within the nodes, and the velocity vector of the fluid particles are limited to a number of directions. PowerFLOW employs D3Q19 model, which considers 19 discrete velocity vectors in 3 dimensions, for solving low Mach number problems [14,30]. The mathematical expression for the lattice-Boltzmann equation is given as follows.

$$F_n(\vec{x} + \vec{V}_n \Delta t, t + \Delta t) - F_n(\vec{x}, t) = \mathbf{C}_n(\vec{x}, t) \quad (2)$$

where  $F_n$  is the particle distribution function in  $n^{\text{th}}$  direction within the lattice,  $\vec{V}_n$  is the discrete particle velocity vector in  $n^{\text{th}}$  direction. The left hand side of Eq. (2) is an expression for time-explicit advection with the increment of  $\vec{V}_n \Delta t$  (spatial) and  $\Delta t$  (temporal). The collision term  $\mathbf{C}_n$  follows that of Bhatnagar-Gross-Krook model [31]:

$$\mathbf{C}_n = -\frac{\Delta t}{\tau} [F_n(\vec{x}, t) - F_n^{\text{eq}}(\vec{x}, t)] \quad (3)$$

where  $\tau$  is the relaxation time which is a function of fluid viscosity and temperature, and  $F_n^{\text{eq}}$  which is the equilibrium distribution function. The single relaxation time is also related to the dimensionless kinematic viscosity as follows [32].

$$\nu = a_s^2 \left( \tau - \frac{\Delta t}{2} \right) \quad (4)$$

Moreover, for low Mach number,  $F_n^{\text{eq}}$  is approximated with a second-order expansion as follows [30].

$$F_n^{\text{eq}} = \rho \omega_n \left[ 1 + \frac{\vec{V}_n \cdot \vec{u}}{a_s^2} + \frac{(\vec{V}_n \cdot \vec{u})^2}{2a_s^4} - \frac{|\vec{u}|^2}{2a_s^2} \right] \quad (5)$$

where  $\omega_n$  are the weighting functions based on the D3Q19 model, and  $a_s = \frac{1}{\sqrt{3}}$  is non-dimensional speed of sound in lattice unit. Eventually, macroscopic flow quantities, such as density  $\rho$  and velocity  $\vec{u}$ , can be recovered after obtaining  $F_n$ .

$$\rho(\vec{x}, t) = \sum_n F_n(\vec{x}, t) \quad (6)$$

$$\rho \vec{u}(\vec{x}, t) = \sum_n \vec{V}_n F_n(\vec{x}, t) \quad (7)$$

For high Reynolds number flows which are common in aerospace applications, the Very Large Eddy Simulation (VLES) model based on two-equations  $k - \epsilon$  Renormalization Group (RNG) [33] is employed for taking into account the sub-grid unresolved turbulence scales. The  $k - \epsilon$  RNG is used to locally adjust the turbulent relaxation time  $\tau_{\text{eff}}$  as follows.

$$\tau_{\text{eff}} = \tau + C_\mu \frac{k^2/\epsilon}{(1 + \eta^2)^{0.5}} \quad (8)$$

where  $C_\mu = 0.09$  and  $\eta$  is based on a local strain parameter ( $k|\bar{S}/\epsilon|$ ), a local vorticity parameter ( $k|\bar{\omega}/\epsilon|$ ), and local helicity parameters. Furthermore, a wall function is applied on the first wall-adjacent grid on a no-slip wall. It is based on the generalized law-of-the-wall model [34], extended to consider the effects of pressure gradient and surface roughness. The wall function is expressed as follows.

$$u^+ = \frac{1}{k} \ln \left( \frac{y^+}{A} \right) + B, \quad (9)$$

where

$$A = 1 + f \left( \frac{dp}{dx} \right), \quad B = 5.0, \quad k = 0.41, \quad y^+ = \frac{u_\tau y}{\nu} \quad (10a-d)$$

and where  $A$  is a function of the pressure gradient.

The LBM scheme is carried out on a lattice of cubic elements which are referred to as *voxels* (i.e., volumetric pixel). The voxel resolution in a certain region can be adjusted depending on the required detail, such that the resolution of voxels in adjacent regions is allowed to vary by a factor of 2. The resolution is specified as a number of voxels assigned for a certain characteristic length (e.g., rod diameter  $D$  in this manuscript). Meanwhile, solid bodies are discretized with planar surfaces, referred to as *surfels* (surface elements), at locations where a voxel intersects with the surface of the body. Furthermore, the fluid particle interaction with the solid surface is governed by the wall boundary condition, such as *particle bounce-back process* for no-slip wall and *specular reflection* for slip wall [32] respectively.

The numerical scheme within LBM is inherently compressible and unsteady. Furthermore, the low dispersion and dissipation properties of LBM allows the acoustic field to be resolved directly within the computational domain (i.e., direct acoustics computation), with a cutoff frequency that corresponds to approximately 15 voxels per wavelength. Due to this requirement, using an acoustic analogy remains a more feasible option for far-field noise computation. For this purpose, PowerFLOW employs Ffowcs-Williams & Hawkings (FW-H) analogy [35] based on Ffarrasat's formulation 1A [36] with forward-time solution [37], extended for permeable surface integration.

## 2.2. The rod-linear cascade model

The present study considers a setup as shown in Fig. 1, which consists of a contraction and a test section housing the rod and the linear cascade. The setup is also intended to be an experimental rig for the Anechoic Vertical Tunnel at Delft University of Technology. The contraction is 1 m long and has a circular inlet with a diameter of 0.6 m and a rectangular outlet of 0.4 m wide and 0.25 m high. Consequently, the test section is designed with the same dimensions as the contraction outlet, with its width equal to the span of the rod and the cascade blades (i.e., 0.4 m). For compensating the flow deflection induced by the linear cascade (i.e.,  $40^\circ$  [38]), the test section includes a curved segment upstream of the RLC, where the inflow is turned of the opposite of the flow deflection angle. This treatment also prevents the outflow of the test section from potentially damaging the walls of the anechoic chamber when an experiment is performed. The curved segment starts at 50 mm downstream of the test section inlet and ends at 180 mm upstream of the rod center. The radius of curvature (i.e., 650 mm) has been carefully chosen to avoid flow separation within the test section.

The cascade profile has been derived from the OGV of the NASA Glenn - Source Diagnostics Test (SDT) rig [39], sampled at  $90^\circ$  of the outer radius. This represents the location where the fan wake-OGV interaction is stronger due to the relatively high mean

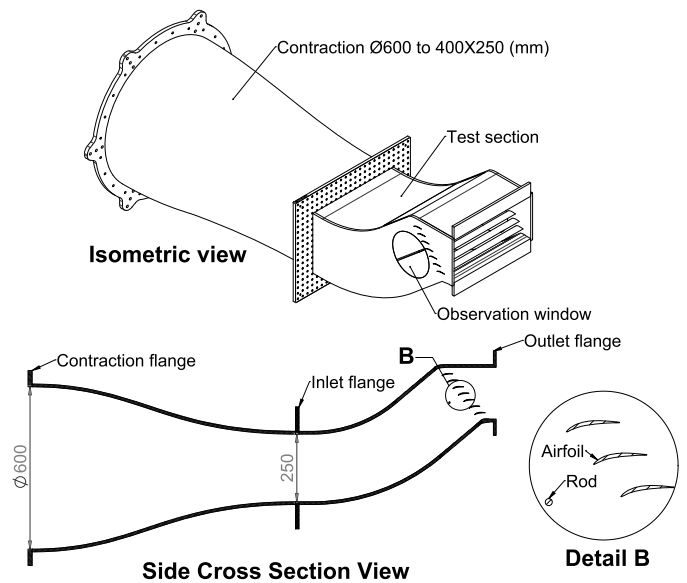
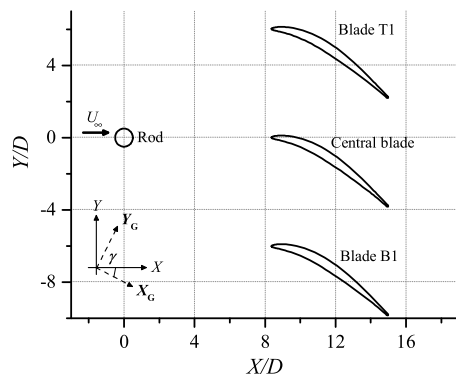


Fig. 1. Technical drawing of rod-linear cascade experiment setup, dimensions are in mm.

velocity, yet the interference from the blade tip remains negligible [38]. The SDT OGV profile is scaled at 1:1 and extruded to obtain a blade that spans 400 mm with constant chord. The solidity ( $\sigma$ ) of the OGV in the SDT rig at the selected radial location is 1.22, which corresponds to the blade-to-blade separation of 32.5 mm. With the given cascade solidity, 7 blades can be accommodated within the test section. The blades are installed at an incidence of  $1^\circ$  to achieve the blade outlet angle as measured from previous numerical studies on the SDT rig [38,40].  $29^\circ$  stagger angle has been chosen to ensure that the blade leading edges are positioned at the identical streamwise distance from the rod. This stagger angle is different than the one applied on the SDT (i.e.,  $11^\circ$ ), however it will be shown later that the loading on the OGV of the RLC and the SDT remain comparable. Additionally, zig-zag tripping elements [40] have been installed on both the pressure and suction sides of the blades at 10% chord length to force laminar-turbulent transition.

The rod is mounted upstream of the cascade with 41 mm separation in between the rod base and the central blade leading edge. The rod has a diameter of  $D = 5.2$  mm such that the mean vortex shedding frequency matches with the first blade-passage-frequency (BPF-1) of the SDT fan stage ( $\approx 2.87$  kHz [39]) at the freestream velocity  $U_\infty$  of 75 m/s. The  $U_\infty$  is chosen to be slightly lower than that measured in the SDT fan stage [38] at approach condition (i.e., 61.7% of maximum RPM) due to the limitation of the wind tunnel facility where the experiment is planned. The resulting Reynolds number based on the rod diameter is  $Re_D = 26600$ , which falls into the shear layer transition regime [41]. Thus, a vortex shedding Strouhal number based on the rod diameter  $St_D$  of around 0.19 – 0.2 is expected [41,42].

A close-up schematic of the rod-linear cascade model is provided in Fig. 2, in which the coordinates have been normalized with the rod diameter  $D$ . The figure also describes two coordinate systems. The first is the local coordinate system ( $X$  and  $Y$ ), whose  $X$  axis is aligned with the inflow vector. The local coordinate system is inclined at  $\gamma = 40^\circ$  against the global coordinate system ( $X_G$  and  $Y_G$ ) whose  $X_G$  is aligned with the cascade outlet angle. Thus,  $\gamma$  is equal to the flow deflection angle induced by the cascade. The  $Z$  axis for both coordinate systems are coinciding and thus does not require separate nomenclature. The local coordinate system should be taken as the default throughout this manuscript unless otherwise specified.



**Fig. 2.** Details on positioning of the rod-linear cascade components with 3 out of the 7 blades are shown.

It is also convenient to define a blade nomenclature system since there are a number of blades to be referred to. The central blade refers to the one whose leading edge is located at  $Y/D = 0$ , while the other blades are given letters (T - top, B - bottom) and numbers (1, 2, and 3 - the higher the number the further away the blade is from the central blade).

### 2.3. Numerical setup

A lateral cutaway of the computational domain is shown in Fig. 3. The simulation domain is a box that is 3.85 m long in the  $X_G$  direction, and 2.6 m in both  $Y_G$  and  $Z_G$  directions. The RLC setup is placed inside the domain such that the contraction inlet coincides with the upstream boundary. The mass flow boundary condition is specified at the contraction inlet to achieve  $U_\infty = 75$  m/s at the contraction exit (i.e., test section inlet). The downstream boundary is an outlet where atmospheric pressure (i.e.,  $p_\infty = 1$  atm) is specified. All of the other boundaries are specified as inlet with zero velocity. Solid bodies, including the contraction, test section, rod, cascade blades, and zig-zag trips, are no-slip walls. An acoustic buffer zone is defined beyond the outer radius of  $100D$  (i.e., the buffer zone boundary is shown in Fig. 3), where the center is located at  $60D$  downstream of the central blade trailing

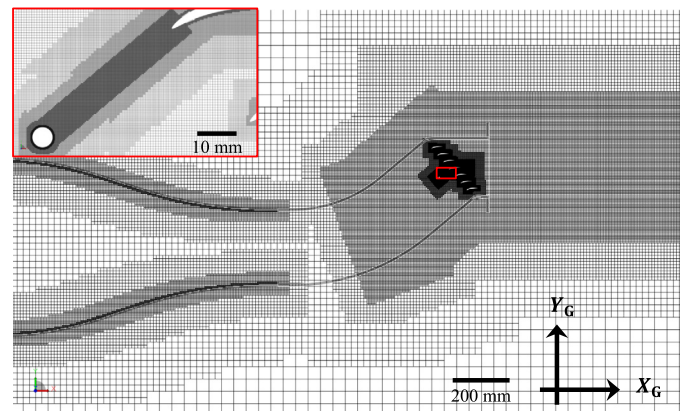


**Fig. 4.** A cut plane showing the grid arrangement at the domain midspan. The inset shows a close-up view on the region bounded by the red box. (For interpretation of the colors in the figure(s), the reader is referred to the web version of this article.)

edge. The buffer zone dampens outward-traveling acoustic waves as well as inward-reflected waves from the domain boundaries.

The domain contains a total of 12 grid refinement regions with the smallest cell size being  $0.016D$ . Consequently, the average  $y^+$  of the first wall-adjacent cell is 8 on the rod and the leading edges of the central blade, blade T1, and blade B1; the  $y^+$  on the other blades is twice as much due to coarser grid resolution. Grid refinement is also performed surrounding the contraction to resolve the boundary layer development upstream of the test section. The discretization strategy results in a total of  $645 \times 10^6$  voxels for the finest grid resolution, and an example of the voxel arrangement surrounding the RLC is shown in Fig. 4. A grid independence study has been performed to verify the convergence trend of the solutions, and it will be discussed in the subsequent section.

Far-field noise computation is performed using a FW-H integration surface that encloses the exterior of the test section, as shown in Fig. 5. Parts of the FW-H surface that intersects with nonquiescent flow field should be removed to eliminate the effects of pseudo-sound (e.g., hydrodynamic fluctuations) [43,44]. These parts are located at 1) upstream of the rod-linear cascade model where the FW-H surface intersects with the test section,

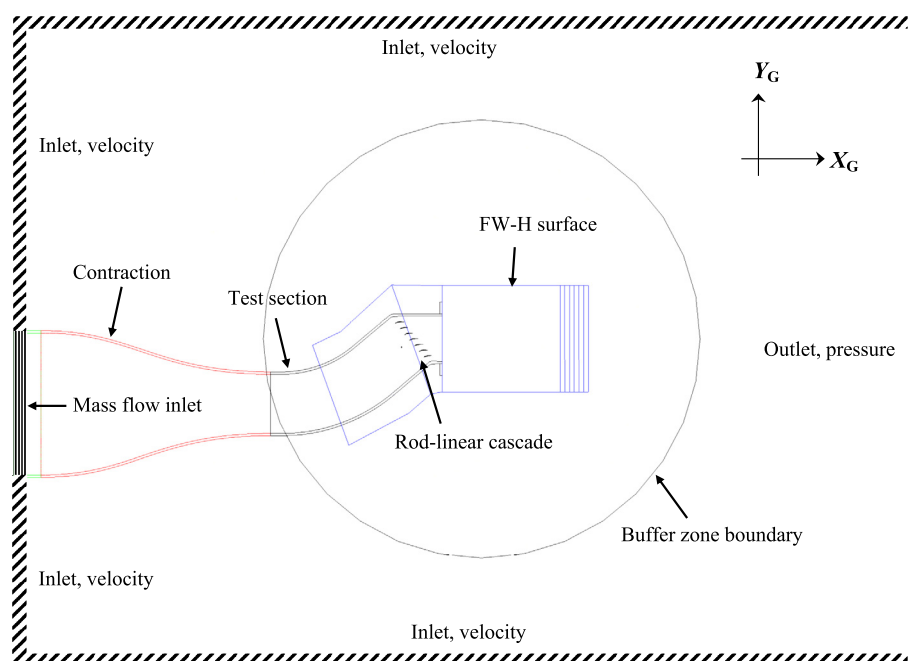


**Fig. 3.** Lateral cutaway of the simulation domain, including boundary conditions specified on the domain boundaries. This figure is not drawn to scale.

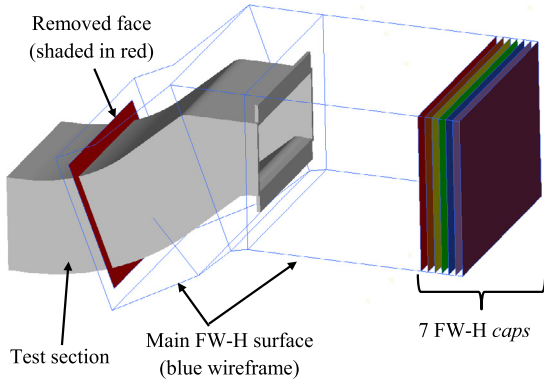


**Fig. 5.** Ffowcs Williams – Hawkins permeable surface setup with 7 caps are shown. The contraction is hidden from the view. The main FW-H surface is shown as wireframe with transparent surface.

and 2) downstream of the test section outlet where the jet shear layer from the test section permeates the FW-H surface. Unfortunately, removal of the latter would reduce the measurement accuracy at shallow angles close to the test section outlet [45,46]. Consequently, the FW-H caps are applied on top of the main permeable surface to filter pseudo-sound contamination. The caps are planar surfaces that are stacked in the streamwise direction with a small separation (i.e., 20 mm or 3.85D) in between. The separation would cause the hydrodynamic fluctuations to be recorded by each cap with temporal lag. This lag is significantly shorter for the passing acoustic waves since the speed of sound is much faster than the convection velocity of the hydrodynamic fluctuations. This results in the pseudo-sound signal to be averaged out during the FW-H computation, while the acoustic ones are preserved.

Subsequently, far-field noise is evaluated on 31 probes that are placed on an arc located at the midplane of the test section. The radius of the arc is 1 m with the origin located at the center of the rod. The arc's zero-angle reference is aligned with positive  $X_C$  axis. The probes are spread across the range of  $[-150^\circ, 150^\circ]$  and an increment of 10 degree. The permeable surface records 2800 samples at 56.5 kHz for 160 vortex shedding cycles (i.e., 56 ms). A Fourier analysis of the acoustics time series is performed using Welch's power spectral density estimate with 50% overlap between FFT bins, resulting in sound spectra with frequency resolution of 51.4 Hz. Unless specified, the power spectral density is normalized in logarithmic scale with reference pressure of 20  $\mu$ Pa, while the frequency is expressed as Strouhal number based on the rod diameter ( $St_D$ ).

After an initial transient, the simulation is carried out for 56.7 ms, which is equivalent to 162 vortex shedding cycle of the rod wake. The total simulation time would allow reliable acoustics measurement for frequencies as low as 300 Hz. All simulations are carried out on a parallel computing facility running 200-core of Intel-Sandybridge Xeon E5-2660.

**2.4. Grid independence study and verification**

A grid independence study has been conducted with three different grid resolutions, namely *coarse*, *medium*, and *fine* with refinement ratio of  $\sqrt{2}$  in between. A summary of the test matrix is provided in Table 1. The convergence trend of the computational domain will be examined based on two aspects of the solution, aerodynamics and far-field acoustics. Unless specified, the results shown has been obtained using the finest grid configuration.

**2.4.1. Aerodynamics of the rod and the central blade**

The spanwise correlation of surface pressure fluctuations on the rod has been observed to affect the statistical behavior of the rod wake [7,42,47], and therefore, should be well-resolved to obtain

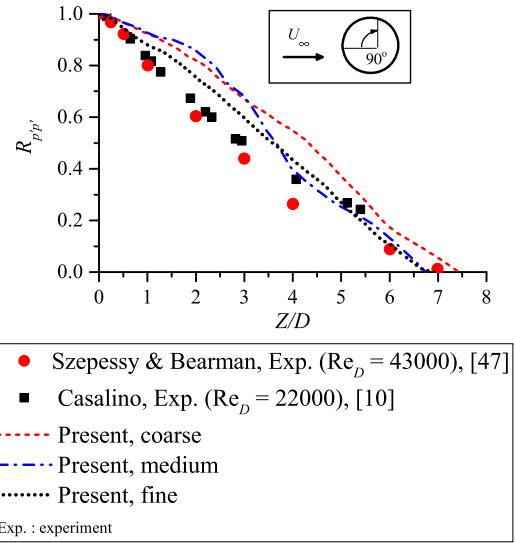


**Fig. 6.** Spanwise correlation of rod surface pressure fluctuation. The rod  $Re_D$  is 26 600 in the present simulation.

**Table 1**

Domain specifications for grid convergence study.

Type	Resolution (voxels/D)	Voxel count ( $10^6$ )	CPU hours ( $10^3$ )
Coarse	62.5	107	7.4
Medium	88.4	300	29.4
Fine	125	645	118

accurate three-dimensional characteristics of the vortex street. The cross-correlation of the surface pressure fluctuation ( $R_{p'p'}$ ) at a location shifted by  $\Delta Z$  relative to a reference location  $Z_{ref}$  is mathematically expressed as follows.

$$R_{p'p'}(Z_{ref} + \Delta Z) = \frac{\langle p'(Z_{ref} + \Delta Z)p'(Z_{ref}) \rangle}{\langle p'(Z_{ref})p'(Z_{ref}) \rangle} \tag{11}$$

where  $p'(Z, t) = p(Z, t) - \bar{p}(Z)$  (i.e., pressure fluctuation surrounding a time-averaged value), and  $\langle \cdot \rangle$  is the ensemble average operator. The reference point  $Z_{ref}$  is located at the midspan of the rod,  $90^\circ$  away from the mean stagnation point.

The results are shown in Fig. 6, in which the spanwise coordinate has been non-dimensionalized with rod diameter  $D$ . The fine case is shown to produce good agreement against other experimental measurements on isolated rod at subcritical Reynolds number range [42,47]. The discrepancies that are present might be attributed to the weak feedback from the airfoil downstream as observed by Jiang et al. [15].

The interaction between the turbulent rod wake and the central blade is reflected by the surface pressure statistics. The grid convergence trends of the mean and root-mean-square (RMS) fluctuations of the surface pressure on the central blade are shown in Fig. 7. The mean pressure coefficient is defined as  $C_{p,mean} = (\bar{p} - p_\infty)/(0.5\rho_\infty U_\infty^2)$ , while the RMS of the pressure fluctuations is normalized as  $p'_{RMS}/(0.5\rho_\infty U_\infty^2)$ . In general, the trend shows consistent results among the three resolution levels, except for the  $p'_{RMS}$  of the coarse case that overpredicts the other results. This might be caused by the insufficient resolution to properly resolve the turbulent structures shed by the tripping elements, since Fig. 7 (ii) shows that the  $p'_{RMS}$  of the coarse simulation matches the others quite well up to  $X/C = 0.1$  where the tripping element is located. This is also evident in Fig. 8 (i) in which a continuous streak of high vorticity region can be observed to originate from the tripping elements. This streak appears to be similar in nature to a shear layer, however, it is not present in both medium and

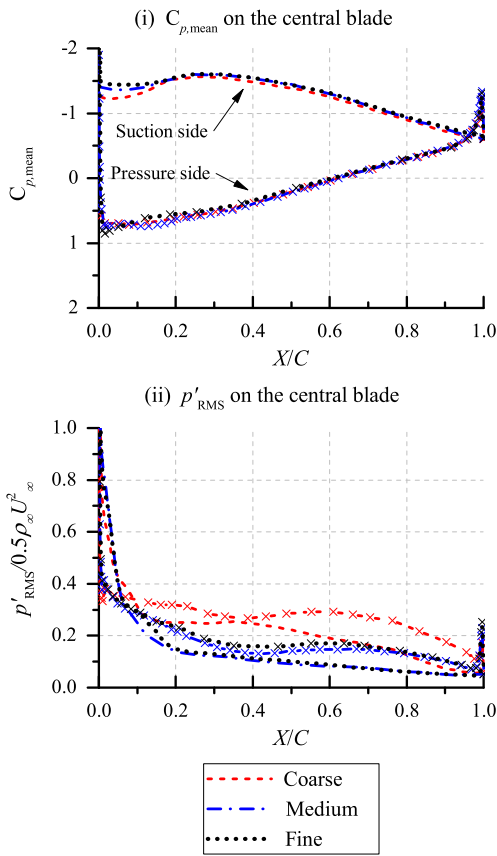


Fig. 7. Mean and fluctuation RMS of surface pressure on the central blade. The distribution on the pressure side is indicated with  $\times$ , while the suction side is unmarked.

fine simulations, resulting in a more similar  $p'_{RMS}$  distribution for both cases.

2.4.2. Far-field acoustics with FW-H analogy

The present study employs FW-H caps to filter pseudo-sound due to the jet shear layer from the test section outlet interacting with the FW-H permeable surface. The FW-H results have been shown to converge as the number of caps is increased [46]. The convergence trend for the RLC setup is shown in Fig. 9 in term of overall sound pressure level (OSPL). When no cap is used, the OSPL is underpredicted in the directions that are close to the normal of the missing cap (e.g.,  $[-30^\circ, 30^\circ]$ ). Conversely, using a single cap results in overprediction due to the additional contribution from the pseudo-sound associated with the jet shear layer coming out from the test section. Nonetheless, the figure shows that 7 caps are sufficient for obtaining converged OSPL at all observation angles.

The sound power level (PWL) can be used to evaluate the effect of varying grid resolution on the overall characteristics of the sound sources. The PWL is evaluated through a summation of

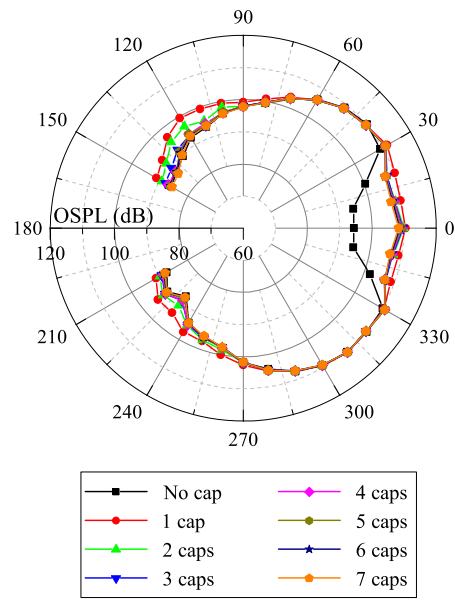


Fig. 9. Effect of the number of FW-H caps on the far-field overall sound pressure level (OSPL).

sound intensity over a spherical dome enclosing the test section. The dome has a radius of 1 m relative to the rod center and it sweeps a full circle in the azimuthal direction but is limited from  $0^\circ$  to  $150^\circ$  in the meridian direction. The dome surface is then discretized into a rectangular grid with a probe located at each vertex with  $10^\circ$  increment. This discretization strategy results in a total of 491 probes.

The PWL spectra in Fig. 10 exhibits good convergence trend, especially between medium and fine cases. The fundamental tone level and the first harmonics are identical across the three grid resolutions. The coarse case, however, shows lower broadband level across the spectra as the corresponding grid resolution is less capable at resolving fine turbulent structures in the rod wake that are responsible for broadband noise generation; this is also clearly shown in Fig. 8. The PWL spectra of the RLC is characterized by a broadband base at around 60 dB, and narrowband peaks surrounding  $St_D = 0.2, 0.4,$  and  $0.6$  that correspond to the fundamental frequency and the harmonics of the rod wake shedding.

The reliability of the FW-H results is also assessed by comparing with acoustic information extracted directly from the computational domain (i.e., direct acoustics computation – DAC). The DAC probes are placed at a radius of 0.6 m from the rod center, which is still located outside of the acoustic buffer zone. The probes acquire 1400 samples at a sampling rate of 28.3 kHz for the same sampling length as the FW-H permeable surface. The results are shown in Fig. 11 where generally good agreement can be observed for various measurement angles. The discrepancy at high frequency ranges is caused by the lower cutoff frequency of the DAC probes,

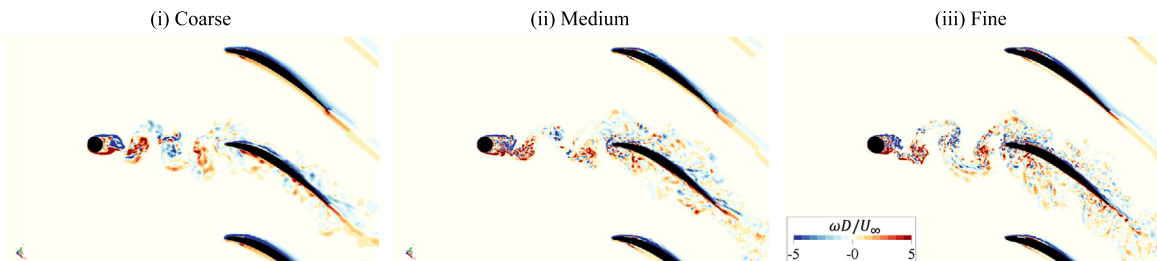
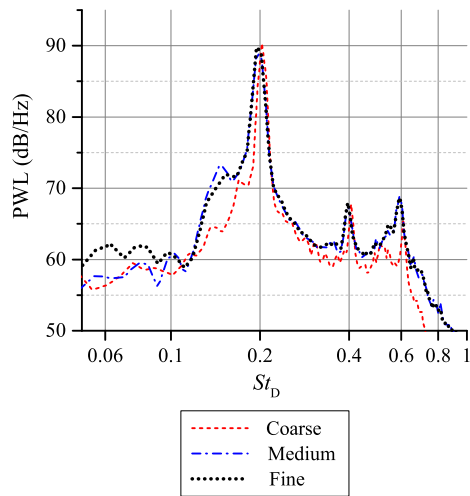


Fig. 8. Comparison of spanwise vorticity ( $\omega_z$ ) contour between various voxel resolution settings. These instantaneous snapshots were taken at approximately the same shedding phase.



**Fig. 10.** The convergence trend of the acoustics source power level (PWL) against various grid resolutions.

since they are located at region with coarser grid resolution compared to that which encloses the FW-H permeable surface.

### 3. Results and discussions

#### 3.1. Velocity field statistics and integral length scales in the rod wake

The mean and RMS statistics of the velocity profile within the test section are shown in Fig. 13. The mean streamwise velocity  $\bar{u}$  and the RMS of the velocity fluctuations  $u'_{RMS}$  are normalized against freestream velocity  $U_\infty = 75$  m/s, and the tangential coordinate with the rod diameter  $D$ . Meanwhile, Fig. 15 shows the velocity fluctuations spectra in selected locations within the test section. These locations are also depicted in Fig. 12.

The velocity profile in the test section upstream of the rod ( $X/D = -7$ ) is shown to be uniform, aside from a small region in proximity of the boundary layer edge at  $Y/D = 20$ , where the mean velocity is 3% higher than  $U_\infty$ . The turbulence intensity along the height of the test section also remains below 1%. The velocity fluctuation spectra at a further upstream location ( $X/D = -10, Y/D = 0$ ) in Fig. 15 shows the peaks corresponding to the rod shedding frequency and its harmonics. This is likely due to acoustic waves from the central blade since the turbulent fluctuations in the area is relatively low.

In Fig. 13 (ii), the rod wake can be identified as the deficit in the mean streamwise velocity, and the increased turbulent fluctuation. An inset in the  $u'_{RMS}$  profile visualizes a pair of peaks that corresponds to the shear layer from the upper and lower sides of the rod. The velocity fluctuation spectra in the rod wake ( $Y/D = 0$ ) is dominated by the broadband components although the tonal peaks are still distinguishable. Outside of the rod wake ( $X/D = 4, Y/D = 15$ ), the broadband level is much lower, similar to that upstream of the rod ( $X/D = -10, Y/D = 0$ ). This also indicates that the peaks in the spectra at these locations are caused by acoustic waves.

The velocity profile inside the cascade channels is presented in Fig. 13 (iii). The RMS velocity plot clearly shows that only the inner channels adjacent to the central blade are influenced by the rod wake; the other channels have very similar mean velocity and turbulent fluctuation profiles (see Fig. 14). This observation is consistent with the spectra in Fig. 15 where the PSD level within the central blade - blade T1 channel ( $X/D = 10, Y/D = 3$ ) is significantly higher than that in the blade T2 - blade T3 channel ( $X/D = 10, Y/D = 15$ ).

Moreover, the PSD level upstream of the blade T2 - blade T3 channel ( $X/D = 4, Y/D = 15$ ) above  $St_D > 0.5$  is also higher than

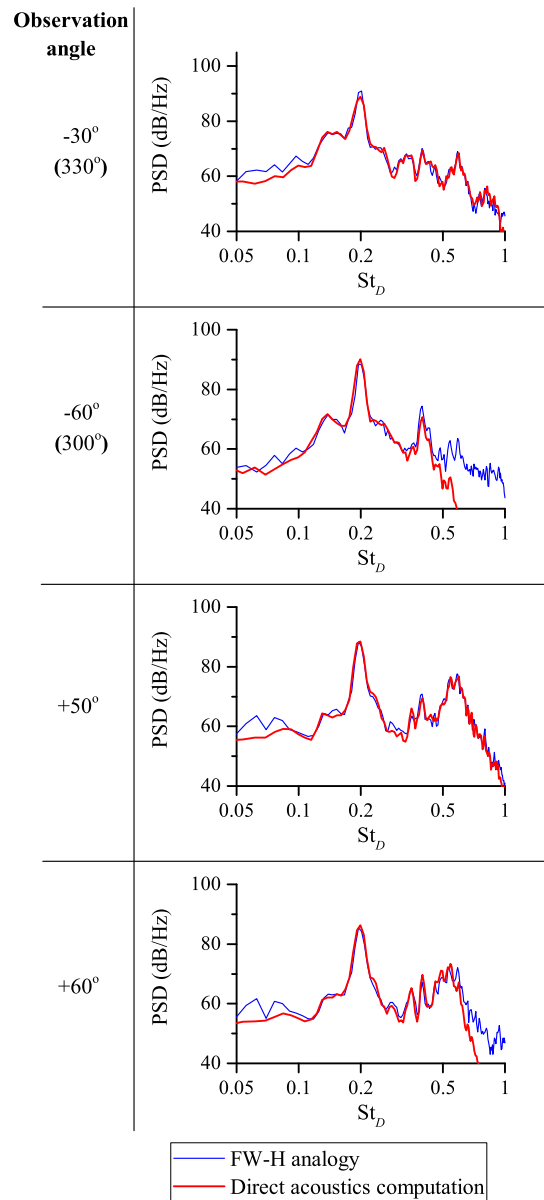


**Fig. 11.** Comparison between results of FW-H and direct acoustics computation for the “fine” grid configuration at various microphone angles and radial distance of 0.6 m.

that inside the channel ( $X/D = 10, Y/D = 15$ ). The discrepancy is likely to be due to the compactness of the acoustic waves relative to the blade chord length. Since the blade chord corresponds to the wavelength at the frequency of  $St_D = 0.58$ , acoustic waves close to or higher than this frequency would be diffracted less efficiently by the cascade blades.

Plot (iv) of Fig. 13 depicts the flow field at the test section outlet. Due to the cascade stagger angle setting, the height of the test section downstream of the cascade is narrower by 30%. Consequently, the mean velocity at the test section outlet becomes significantly higher than  $U_\infty$ . The influence of the rod wake can still be observed at this location as the bump surrounding  $Y/D = 0$  in the RMS velocity plot. The velocity fluctuation spectra at the center of the outlet is shown to be broadband in Fig. 15, implying that the coherence of the large scale vortices in the rod wake is lost after impinging the central blade.

Spanwise vorticity ( $\omega_z$ ) contour and  $\lambda_2$  [48] iso-surface are shown in Fig. 16 to illustrate the instantaneous flow field in proximity of the rod and the central blade. The rod sheds turbulent

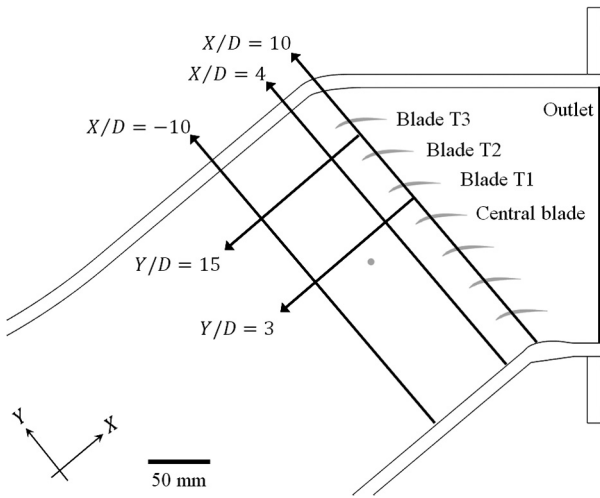


Fig. 12. Sampling locations of velocity statistics shown in Fig. 13 and 15.

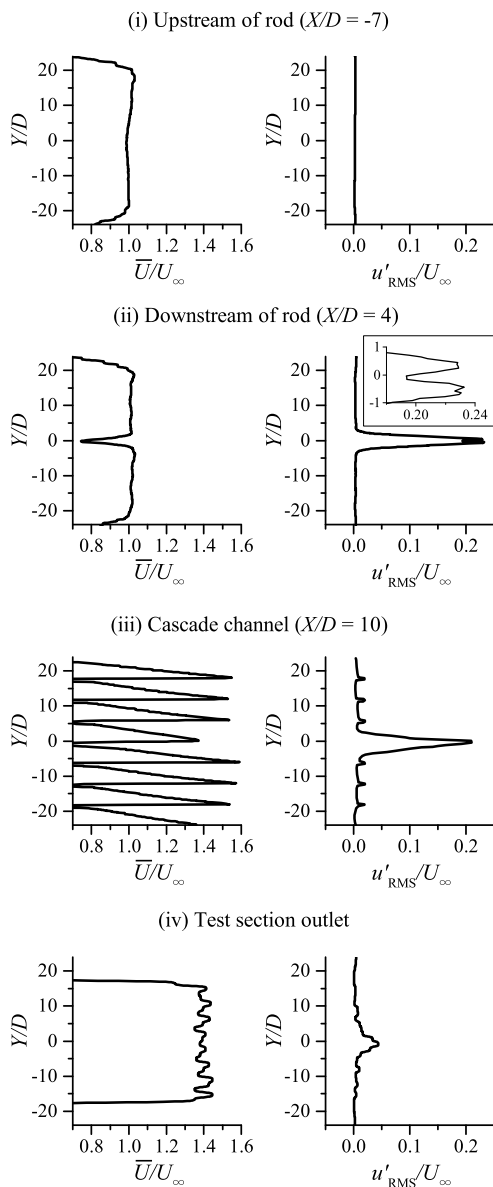


Fig. 13. Profiles of mean axial velocity ( $\bar{U}/U_\infty$ ) and root-mean-square of velocity fluctuations ( $u'_{RMS}/U_\infty$ ) measured at various stations throughout the midspan of the test section ( $Z/D = 0$ ).

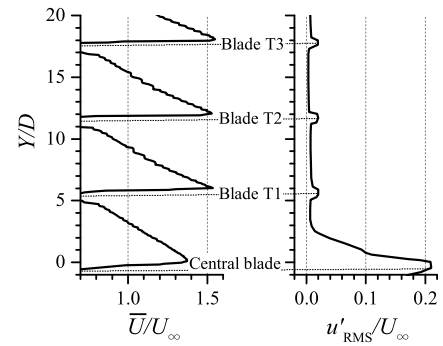


Fig. 14. A closer look at the velocity profiles of Fig. 13 (iii). The locations of each blade are also indicated.

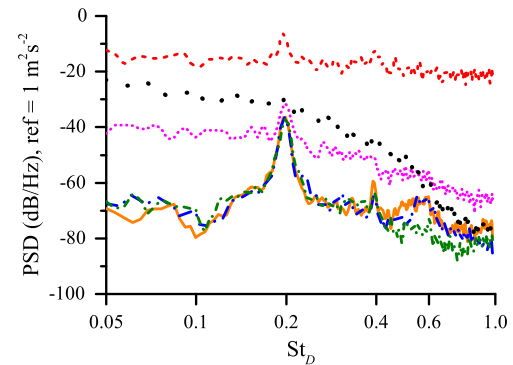


Fig. 15. Power spectral density of streamwise velocity fluctuation at the midspan of the test section.

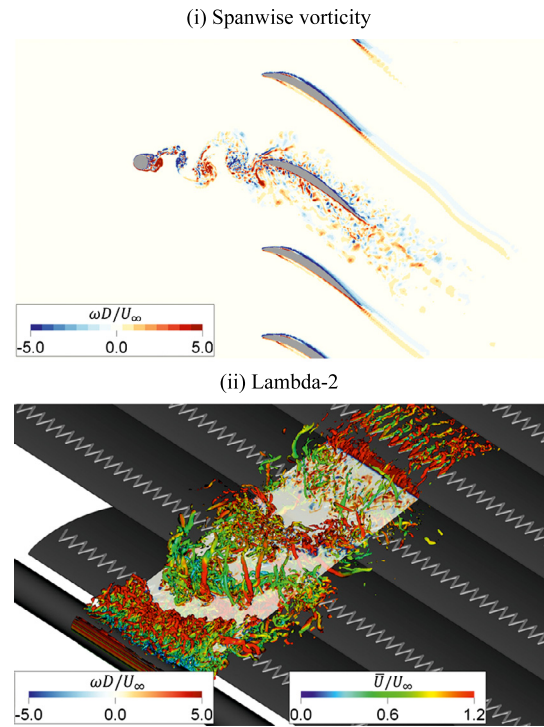
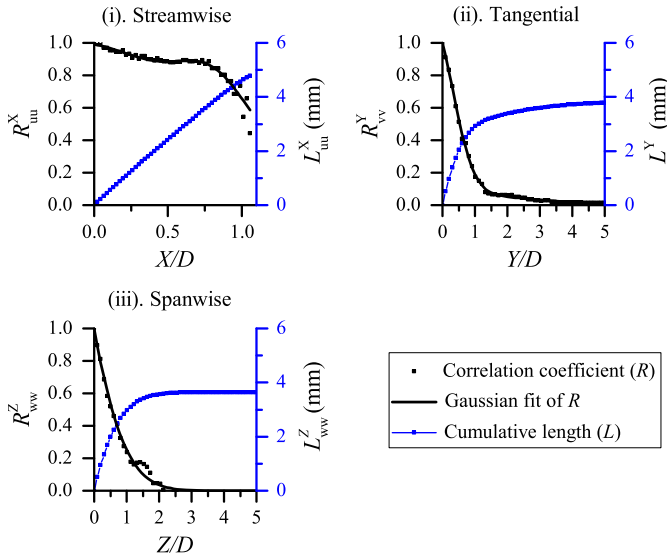


Fig. 16. Instantaneous contour of spanwise vorticity ( $\omega_z$ ) at the midspan and lambda-2 iso-surface ( $\lambda_2 = -3 \times 10^9 \text{ s}^{-2}$ ) with  $y = 0$  plane included for highlighting the wake pattern. The iso-surface is shown up to  $\pm 5D$  in the spanwise direction. Both contours correspond to the same time instance.



**Fig. 17.** Cross-correlation coefficients  $R_{ij}^m(\vec{x})$  of the three velocity fluctuation components and the cumulative length at  $2D$  upstream of the central blade.

**Table 2**

The integral length scales of within the rod wake at  $D$  distance upstream of the central blade leading edge.

	Present	Podboy et al. [52] <sup>+</sup>	Casalino et al. [51] <sup>+</sup>
$L_{uu}^x$	4.78 mm	4.65 mm	6.50 mm
$L_{vv}^y$	3.78 mm	–	4.50 mm
$L_{wv}^z$	3.64 mm	–	6.80 mm

<sup>+</sup> Hotwire measurement inside the NASA SDT rig.

<sup>+</sup> LBM/VLES simulation of the NASA SDT rig.

vortices which are then impinging the leading edge of the central blade. The vortices are severely deformed and broken down into small eddies as they interact with the leading edge, producing sound in the process as described by Powell’s analogy [49]. Fig. 16 also shows that the unsteady rod wake does not appear to contaminate the flow field in the cascade channels except the two next to the central blade.

The turbulent wake impinging on the central blade leading edge can be characterized using the integral length scales  $L^m$  in  $m^{\text{th}}$  direction, using the estimation procedure based on cross-correlation proposed by Gea Aguilera et al. [50]. The integral length scales are expressed as in Eq. (12). The same method was also applied in similar studies [40,51,46].

$$L_{ij}^m(\vec{x}) = \int_0^\infty R_{ij}^m(\vec{x}) d\vec{x} \tag{12}$$

$$= \int_0^\infty \frac{\langle u_i'(\vec{x} + s\vec{e}_m)u_j'(\vec{x}) \rangle}{\langle u_i'(\vec{x})u_j'(\vec{x}) \rangle} d\vec{x}$$

where  $R_{ij}^m(\vec{x})$  is the correlation coefficient between the time series at locations along  $\vec{x}$ ,  $u_i'$  and  $u_j'$  are the turbulent velocity fluctuation components in  $i^{\text{th}}$  and  $j^{\text{th}}$  directions respectively,  $e_m$  is the unitary vector in  $m^{\text{th}}$  direction,  $s$  is the separation from a reference location  $\vec{x}$ , and  $\langle \cdot \rangle$  is the ensemble-averaging operator.

The cross-correlation is computed based on a reference position located at  $D$  distance upstream of central blade leading edge. From the reference position, 50 points are spread along the positive streamwise ( $X$ ), tangential ( $Y$ ), and radial ( $Z$ ) directions. The separation between each point is  $0.02D$  in the streamwise direc-

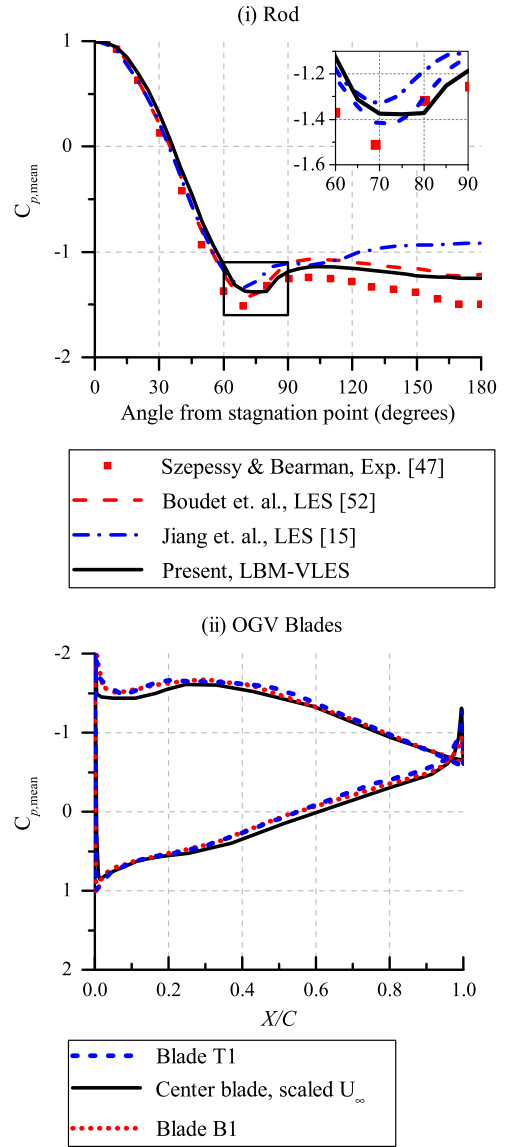


**Fig. 18.** Mean surface pressure distribution at the midspan of the rod and the cascade blades.

tion and  $0.1D$  in both the tangential and radial directions. Afterward, 1600 samples of the corresponding velocity fluctuations are retrieved at 28.6 kHz from each point.

The results of Eq. (12) are shown in Fig. 17 and the length scales are summarized in Table 2. The results are also compared to other studies conducted with the NASA-Glenn SDT fan stage [51, 52]. It is important to note, however, that the length scale estimate of Podboy et al. [52] is based on the averaging of velocity fluctuation spectra at a given location (i.e., autocorrelation) in the limit of zero frequency. This estimate was considered to be unsuitable in the present study due to the fact that the sampling time of a simulation is typically much shorter than that of an experiment, which would lead to unreliable spectral averaging at the low frequency ranges. Casalino et al. [51] also used the cross-correlation procedure and found that their results overestimate that of Podboy et al. Nevertheless, all results show similar order of magnitude and trend, e.g., the length scale in the axial direction is longer than in the other directions. This information would be useful for designing relevant noise mitigation technique, such as the leading edge serrations [50,51,53].

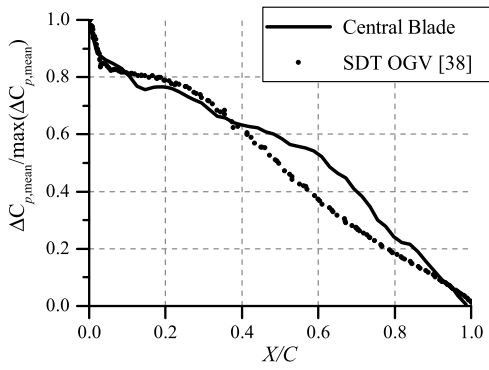


Fig. 19. Comparison of the distribution of the surface pressure difference between pressure side and suction side of the RLC central blade and the NASA SDT OGV.

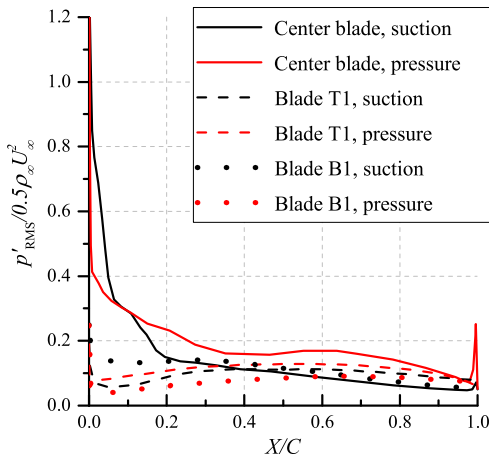


Fig. 20. RMS surface pressure distribution on the central blade, blade T1, and blade B1.

3.2. Surface pressure statistics

The mean surface pressure coefficient on both the rod and the airfoil are shown in Fig. 18. Jiang et al. [15] has previously observed that as the separation between the rod and the downstream body becomes larger than  $6D$ , the rod pressure distribution approaches that of an isolated rod. This is consistent with the present result in Fig. 18 (i) since the rod-central blade separation is  $8D$  in present case. The rod of the RLC also show very similar pressure distribution compared to that of the RAC [15,54], which may imply that the cascade of the RLC does not affect the rod differently than that of the RAC.

The mean pressure coefficient of the central blade is compared with the adjacent blades (i.e., blade T1 and B1) in Fig. 18 (ii). The freestream velocity used for normalizing the surface pressure of the central blade, however, is  $0.9U_{\infty}$ . This is obtained by time-averaging the streamwise velocity component at  $2D$  upstream of the central blade leading edge. The resulting scaled pressure coefficient resembles that of the T1 and B1 blade, which is consistent with the observations in previous section that the rod wake causes momentum deficit in the flow field surrounding the central blade.

It is also interesting to compare the loading characteristics of the central blade to the OGV of the SDT fan stage since the purpose of using a detailed geometry is to approach the realistic operating condition as close as possible. This comparison is provided in Fig. 19 in term of  $\Delta C_{p,mean}$ , which is the difference of pressure coefficient between the pressure and suction sides of the blade (Eq. (13)).  $\Delta C_{p,mean}$  is then normalized with the maximum value for each respective case (i.e.,  $\max(\Delta C_{p,mean})$ ).

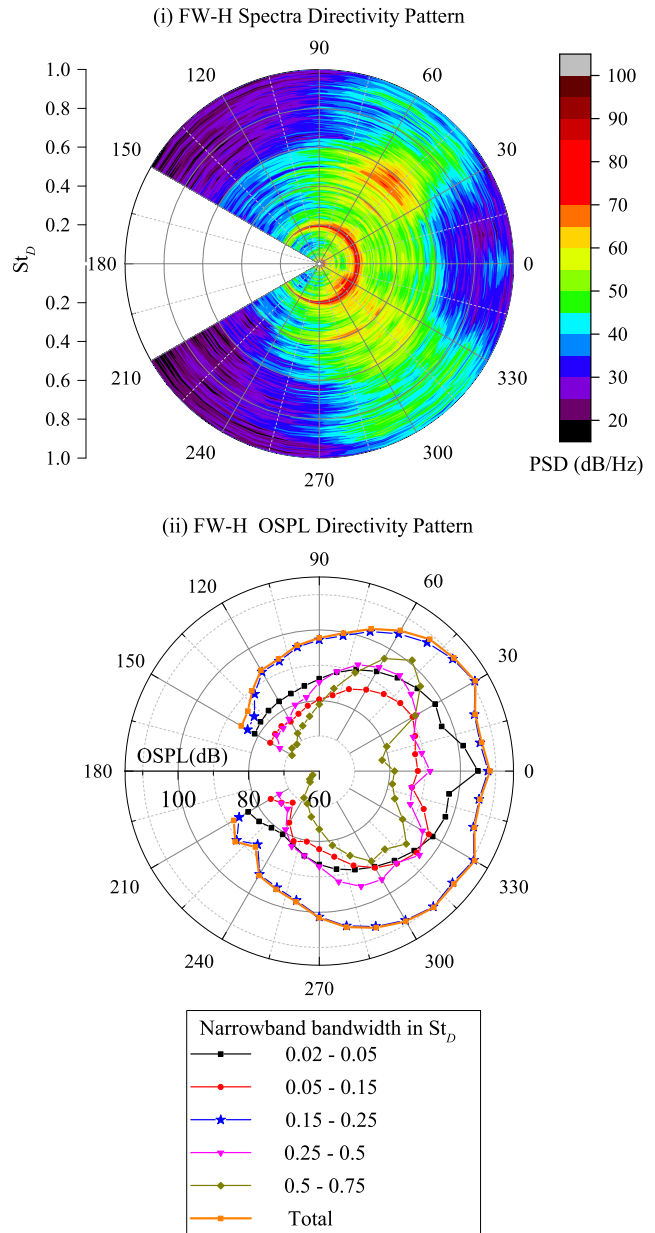


Fig. 21. Far-field sound spectra and OSPL directivity pattern measured at an arc along the midplane of the test section.

Table 3 Mean and fluctuation statistics of lift and drag coefficients of the RLC components.

	$C_{L,mean}$	$C_{D,mean}$	$C'_{L,RMS}$	$C'_{D,RMS}$
Rod	$\approx 0$	1.22	0.16	0.019
Central blade	1.18	0.52	0.16	0.066
Blade T1	1.53	0.64	0.11	0.051
Blade B1	1.54	0.64	0.12	0.069
Blade T2	1.52	0.65	0.07	0.035
Blade B2	1.54	0.66	0.10	0.059

$$\Delta C_{p,mean} = C_{p,mean}|_{pressure} - C_{p,mean}|_{suction} \tag{13}$$

The comparison shows acceptable agreement except at  $X/C = 0.2$  and at downstream of  $X/C = 0.4$ . The former may have been caused due to the tripping element used in the RLC, while the latter could be associated with the discrepancy in the flow field characteristics downstream of the blade mid-chord due to different stagger angle settings.

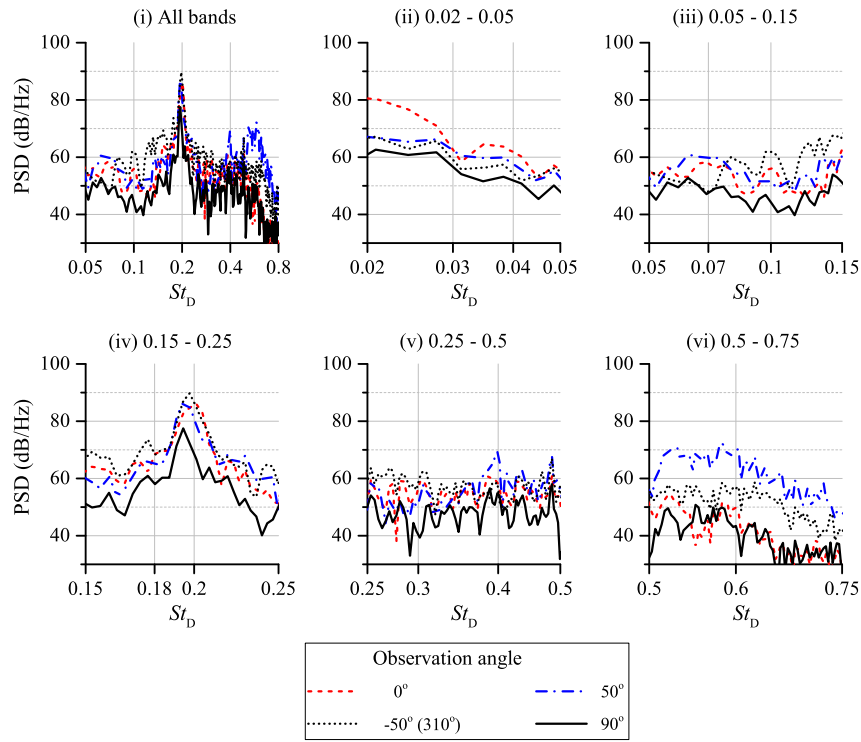


Fig. 22. Far-field sound spectra at selected directions. Plots (ii) to (v) provide zoomed view at frequency bands as specified in Fig. 21.

The surface pressure fluctuations distribution is illustrated in Fig. 20, where  $p'_{\text{RMS}}$  has been normalized with  $0.5\rho_{\infty}U_{\infty}^2$ . As expected, the rod wake causes high level of pressure fluctuation at the central blade leading edge. Nonetheless, the fluctuation intensity decreases immediately further downstream, which indicates that the unsteady loading associated with the rod wake impingement is localized at the leading edge region. Another spike is also observed nearby the central blade trailing edge which might be caused by the turbulent structures over the central blade interacting with the trailing edge. Meanwhile, the pressure fluctuation level on the blade T1/B1 is significantly lower, although closer comparison reveals that the sides of the blades that are facing the central blade (e.g., pressure side of blade T1 and suction side of blade B1) experience slightly higher level compared to the opposite sides.

A summary on the aerodynamic forces statistics of the RLC components are provided in Table 3. The forces are expressed as lift and drag coefficients with respect to the local coordinate system. The rod  $C_{D,\text{mean}}$  is within the expectation of an isolated rod [41,47] and the rod in the RAC [15]. The mean lift and drag on all blades are almost identical, except for the central blade that is under the rod wake influence. On the other hand, the RMS forces on the inner blades (i.e., T1/B1) is slightly higher than that of the outer ones (i.e., T2/B2). Consistent with the observation on  $p'_{\text{RMS}}$  distributions in Fig. 20, this implies that the aerodynamic influence of the rod wake is limited only to the channels neighboring the central blade.

### 3.3. Acoustics analyses

Unlike the RAC, the sound propagation from the central blade in the RLC is heavily influenced by the usage of the cascade and the test section. This is elaborated further by the far-field sound spectra in Fig. 21 (i) and Fig. 22, and bandwidth-filtered directivity pattern in Fig. 21 (ii). Furthermore, the dilatation field ( $\nabla \cdot \vec{u}$ ) and RMS pressure fluctuation ( $p'_{\text{RMS}}$ ) contours in Fig. 23 and 24 provide acoustic field visualization surrounding the RLC. The dilatation

field is expressed in term of time derivative of pressure as shown in Eq. (14) [55].

$$\nabla \cdot \vec{u} = -\frac{1}{\rho_{\infty}c_{\infty}^2} \frac{\partial p}{\partial t} \quad (14)$$

where  $\rho_{\infty}$  and  $c_{\infty}$  are freestream density and speed of sound respectively. Afterward,  $\frac{\partial p}{\partial t}$  is normalized using freestream dynamic pressure (i.e.,  $0.5\rho_{\infty}U_{\infty}^2$ ) and the characteristic time (i.e.,  $D/U_{\infty}$ ).

The lowest frequency band (i.e.,  $0.02 < St_D < 0.05$ ) is mainly associated with the fluctuations inside the shear layer at the test section outlet, which can be clearly observed in Fig. 23 (i) and Fig. 24 (i). Nevertheless, the fluctuations are not present in other higher frequency bands, implying that the sound from the shear layer is restricted to the low frequency ranges.

The frequency band surrounding the fundamental shedding frequency (i.e.,  $0.15 < St_D < 0.25$ ) is shown to dominate the spectra. The sound source of this band corresponds to the periodic upwash-downwash fluctuations in the rod vortex street as shown in Fig. 23 (ii), which are scattered by the central blade leading edge. Subsequently, sound waves are propagated into the adjacent channels, diffracted by the neighboring blades before impinging the ceiling and the floor of the test section. The acoustic-blade interaction of this frequency band is also responsible for the high  $p'_{\text{RMS}}$  level within the inter-blade channels as shown in Fig. 24 (ii). This phenomenon may be similar in nature to the cascade resonance within the inter-blade channels as observed by Parker [56] and more recently by Yokoyama et al. [57]. Nevertheless, the  $p'_{\text{RMS}}$  in the channels further away from the central blade is lower than the closer ones since the aerodynamic excitation is limited only to the central blade, unlike the case of Parker and Yokoyama in which the entire cascade is excited due to vortex shedding from each blade.

The smaller eddies within the rod wake are responsible for the noise generation at higher Strouhal bands (i.e.,  $St_D > 0.25$ ), as depicted in Fig. 23 (iii). These frequency bands exhibit stronger radiation toward the upper arc in contrast with the lower and mid frequency bands. While the reason for this behavior remains

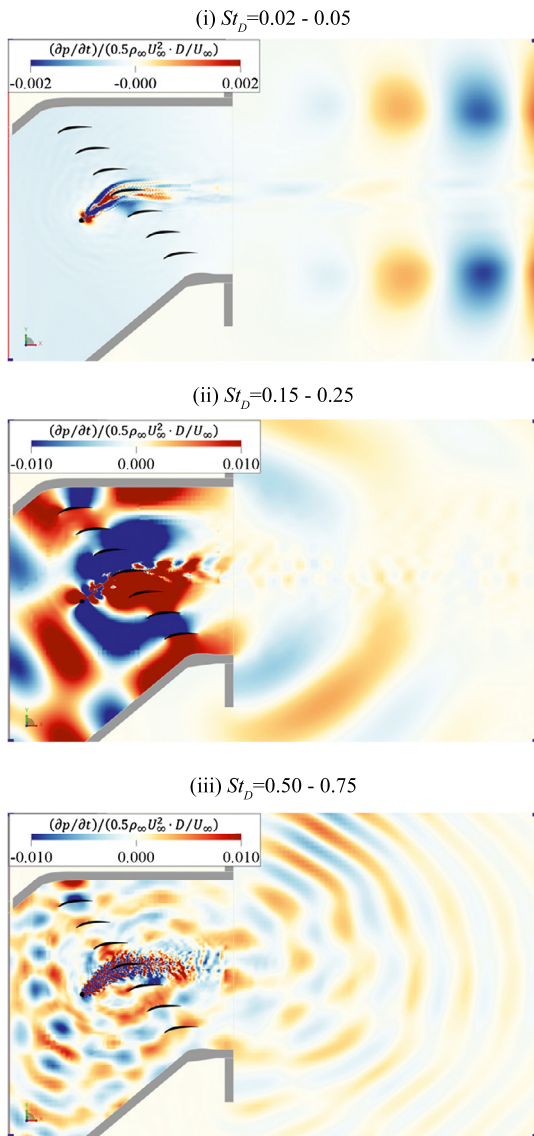


**Fig. 23.** Bandpass-filtered contour of instantaneous dilatation field in term of time derivative of pressure.

unclear, it might be associated with the cascade stagger setting and the influence of the acoustic wave compactness relative to the blade-to-blade separation, which in turn affects the duct mode radiation from each cascade channel [23]. The high  $p'_{RMS}$  regions remain present in the frequency band of  $0.5 > St_D > 0.75$  (i.e., Fig. 24 (iii)), although the extent of the regions is smaller, i.e., limited to the channels adjacent to the central blade.

The directivity of the sound coming out of the test section outlet is relatively uniform at low frequency ranges up to  $St_D = 0.05$ . Above this frequency, the directivity starts to take cardioid shape with the preference towards the lower arc for  $0.05 > St_D > 0.5$ . This is clearly shown in Fig. 22 (iv) in which the peak at  $St_D = 0.19$  is around 5 dB higher at  $-50^\circ$  compared to at  $50^\circ$ . Nonetheless, this trend reverses for frequency ranges above  $St_D > 0.5$  where the broadband sound distribution is generally higher towards the upper arc (i.e., in Fig. 22 (vi)). These asymmetrical radiation behaviors might be related to the geometrical aspects of the cascade itself (e.g., blade camber and stagger angle) [22,23,58], and these are also interesting aspects of the RLC to be verified in the future experimental study.

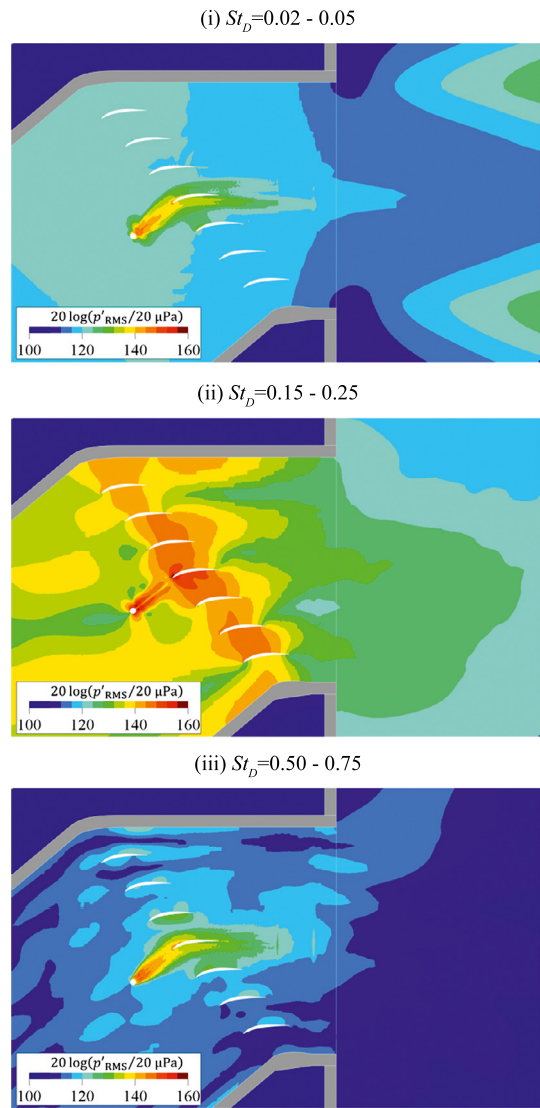


**Fig. 24.** Bandpass-filtered contour of RMS of pressure fluctuation in decibel scale.

#### 4. Conclusion and outlook

This manuscript has presented a numerical study on the aerodynamics and aeroacoustics characteristics of the rod-linear cascade model (RLC). The flow field was solved using unsteady, explicit solver based on lattice-Boltzmann method, while the far-field noise was computed using the Ffowcs-Williams and Hawkins analogy. A grid independence study has been performed to ensure the robustness of the present numerical solutions.

The rod has been designed to shed turbulent vortex street with a fundamental frequency that equal to the 1<sup>st</sup> BPF of the NASA-Glenn SDT fan stage at *approach* condition. The cascade profile and solidity are also derived from the SDT, which allowed 7 blades to be used inside a rectangular test section. The test section has been equipped with a curved segment upstream of the RLC to compensate the flow deflection produced by the cascade. Nonetheless, flow field assessment revealed that the velocity distribution has become sufficiently uniform with relatively low turbulent intensity at the rod location.

The rod shed turbulent wake that impinged onto the central blade leading edge. The integral length scales within the rod wake were measured and found to follow the trend observed in the SDT fan stage, despite the streamwise length scale being significantly underpredicted. The rod wake impingement process induced

strong unsteady pressure fluctuations on the central blade leading edge, which are subsequently scattered as sound waves.

Surface pressure measurements on the rod revealed that the central blade did not cause significant feedback between the two bodies. However, the mean loading on the central blade was lower compared to the other blades due to the momentum deficit induced by the rod wake. Nevertheless, by using normalization based on the lower mean velocity in the rod wake, the central blade and the adjacent blades were found to have similar loading characteristics. Consistently, the mean forces acting on the blades, except the central blade, were identical, while the forces RMS were slightly higher for those located next to the central blade.

Acoustic analyses have shown that the installation and cascade effects have a significant influence on the far-field sound characteristics. The frequency band surrounding the fundamental shedding frequency dominated the sound spectra in all measured directions, whereas the installation effect associated with the jet shear layer at the test section outlet was limited to the low frequency ranges. Furthermore, the cascade effects caused high pressure fluctuation inside the inter-blade channels, including those that are not directly perturbed by the rod wake. The pressure fluctuation level was observed to be lower in channels further away from the central blade, as well as at higher frequency ranges.

To conclude, the RLC is a system that couples two aeroacoustics phenomena, namely the leading edge noise generation by interaction with oncoming turbulence, and the acoustics-blade interactions due to the usage of high solidity cascade. Since these phenomena are inherent in fan wake-OGV interaction mechanism, the RLC presents the opportunity as a test rig for exploring novel noise mitigation techniques for applications in future turbofans. It is also conjectured that noise reduction within the RLC could be achieved with the following mechanisms: 1) dampening the surface pressure fluctuation at the leading edge (e.g., with porous materials [59]), 2) enhancing decorrelation or phase interference effects of the turbulence impingement process (e.g., with leading edge serrations [53]), and 3) reducing the cascade effects (e.g., with acoustic treatment on the blade surface [60]). Furthermore, future studies using the RLC would also allow elucidating the impact of various noise mitigation strategies on the OGV performance since the geometrical details are preserved.

## Declaration of Competing Interest

The author(s) declare(s) that there is no conflict of interest regarding the publication of this article.

## Acknowledgement

This study is supported by the project SMARTANSWER (Smart Mitigation of flow-induced Acoustic Radiation and Transmission for reduced Aircraft, surface transport, Workplaces and wind energy noise) which has received funding from the European Union's Horizon 2020 research and innovation program under the Marie Skłodowska-Curie grant agreement No. 722401. More information can be found on <https://www.h2020-smartanswer.eu/>.

## References

- [1] J.M. Tyler, T.G. Sofrin, Axial Flow Compressor Noise Studies, Tech. rep., SAE Technical Paper, 1962.
- [2] J. Groeneweg, E.J. Rice, Aircraft turbofan noise, *J. Turbomach.* 109 (1) (1987) 130–141.
- [3] D. Casalino, F. Diozzi, R. Sannino, A. Paonessa, Aircraft noise reduction technologies: a bibliographic review, *Aerosp. Sci. Technol.* 12 (1) (2008) 1–17.
- [4] D. Lockard, M. Khorrami, M. Choudhari, F. Hutchison, T. Brooks, D. Stead, Tandem cylinder noise predictions, in: 13th AIAA/CEAS Aeroacoustics Conference (28th AIAA Aeroacoustics Conference), 2007, p. 3450.
- [5] D. Lockard, Summary of the tandem cylinder solutions from the benchmark problems for airframe noise computations-I workshop, in: 49th AIAA Aerospace Sciences Meeting Including the New Horizons Forum and Aerospace Exposition, 2011, p. 353.
- [6] G.A. Bres, D. Freed, M. Wessels, S. Noelting, F. Pérot, Flow and noise predictions for the tandem cylinder aeroacoustic benchmark, *Phys. Fluids* 24 (3) (2012) 036101.
- [7] M.C. Jacob, J. Boudet, D. Casalino, M. Michard, A rod-airfoil experiment as a benchmark for broadband noise modeling, *Theor. Comput. Fluid Dyn.* 19 (3) (2005) 171–196.
- [8] J. Giesler, E. Sarraj, Measurement of broadband noise generation on rod-airfoil-configurations, in: 15th AIAA/CEAS Aeroacoustics Conference (30th AIAA Aeroacoustics Conference), 2009, p. 3308.
- [9] S.R.L. Samion, M.S.M. Ali, A. Abu, C.J. Doolan, R.Z.-Y. Porteous, Aerodynamic sound from a square cylinder with a downstream wedge, *Aerosp. Sci. Technol.* 53 (2016) 85–94.
- [10] D. Casalino, Analytical and Numerical Methods in Vortex-Body Aeroacoustics, Ph.D. thesis, Politecnico di Torino et Ecole Centrale de Lyon, 2002.
- [11] B. Greschner, F. Thiele, M.C. Jacob, D. Casalino, Prediction of sound generated by a rod-airfoil configuration using EASM DES and the generalised Lighthill/FW-H analogy, *Comput. Fluids* 37 (4) (2008) 402–413.
- [12] J.-C. Giret, A. Sengissen, S. Moreau, M. Sanjosé, J.-C. Jouhaud, Noise source analysis of a rod-airfoil configuration using unstructured Large-Eddy simulation, *AIAA J.* 53 (4) (2015) 1062–1077.
- [13] J.-C. Giret, A. Sengissen, S. Moreau, M. Sanjosé, J.-C. Jouhaud, Prediction of the sound generated by a rod-airfoil configuration using a compressible unstructured LES solver and a FW-H analogy, in: 18th AIAA/CEAS Aeroacoustics Conference (33rd AIAA Aeroacoustics Conference), 2012, p. 2058.
- [14] R. Satti, P.-T. Lew, Y. Li, R. Shock, S. Noelting, Unsteady flow computations and noise predictions on rod-airfoil using lattice Boltzmann method, in: 47th AIAA Aerospace Sciences Meeting Including the New Horizons Forum and Aerospace Exposition, 2009, p. 497.
- [15] Y. Jiang, M.-L. Mao, X.-G. Deng, H.-Y. Liu, Numerical investigation on body-wake flow interaction over rod-airfoil configuration, *J. Fluid Mech.* 779 (2015) 1–35.
- [16] W. Chen, W. Qiao, F. Tong, L. Wang, X. Wang, Numerical investigation of wavy leading edges on rod-airfoil interaction noise, *AIAA J.* (2018) 1–15.
- [17] S.A.L. Glegg, Airfoil self-noise generated in a cascade, *AIAA J.* 36 (9) (1998) 1575–1582.
- [18] H.H. Hubbard, Aeroacoustics of Flight Vehicles: Theory and Practice. Volume 1. Noise Sources, Tech. rep. NASA Langley Research Center, Hampton, VA, 1991.
- [19] A. Finez, M. Jacob, E. Jondeau, M. Roger, Experimental investigation of trailing-edge noise from a linear cascade of cambered airfoils, in: 17th AIAA/CEAS Aeroacoustics Conference (32nd AIAA Aeroacoustics Conference), 2011, p. 2876.
- [20] R.K. Amiet, Noise due to turbulent flow past a trailing edge, *J. Sound Vib.* 47 (3) (1976) 387–393.
- [21] N. Peake, E. Kerschen, Influence of mean loading on noise generated by the interaction of gusts with a flat-plate cascade: upstream radiation, *J. Fluid Mech.* 347 (1997) 315–346.
- [22] I. Evers, N. Peake, On sound generation by the interaction between turbulence and a cascade of airfoils with non-uniform mean flow, *J. Fluid Mech.* 463 (2002) 25–52.
- [23] N. Peake, E. Kerschen, Influence of mean loading on noise generated by the interaction of gusts with a cascade: downstream radiation, *J. Fluid Mech.* 515 (2004) 99–133.
- [24] S.M. Grace, Influence of model parameters and the vane response method on a low-order prediction of fan broadband noise, *Int. J. Aeroacoust.* 15 (1–2) (2016) 131–143.
- [25] J. de Laborde, V. Blandeau, T. Node-Langlois, S. Moreau, Extension of a fan tonal noise cascade model for camber effects, *AIAA J.* 53 (4) (2014) 863–876.
- [26] H. Posson, S. Moreau, M. Roger, On the use of a uniformly valid analytical cascade response function for fan broadband noise predictions, *J. Sound Vib.* 329 (18) (2010) 3721–3743.
- [27] L. Soulat, S. Moreau, H. Posson, Wake model effects on the prediction of turbulence-interaction broadband noise in a realistic compressor stage, in: 41st AIAA Fluid Dynamics Conference and Exhibit, 2011, p. 3900.
- [28] S.R. Kumar, A. Sharma, A. Agrawal, Simulation of flow around a row of square cylinders, *J. Fluid Mech.* 606 (2008) 369–397.
- [29] S. Succi, The Lattice Boltzmann Equation: For Fluid Dynamics and Beyond, Oxford University Press, 2001.
- [30] H. Chen, S. Chen, W.H. Matthaeus, Recovery of the Navier-Stokes equations using a lattice-gas Boltzmann method, *Phys. Rev. A* 45 (8) (1992) R5339.
- [31] P.L. Bhatnagar, E.P. Gross, M. Krook, A model for collision processes in gases. I. Small amplitude processes in charged and neutral one-component systems, *Phys. Rev.* 94 (3) (1954) 511.
- [32] H. Chen, C. Teixeira, K. Molvig, Realization of fluid boundary conditions via discrete Boltzmann dynamics, *Int. J. Mod. Phys. C* 9 (08) (1998) 1281–1292.
- [33] V. Yakhot, S.A. Orszag, Renormalization group analysis of turbulence. I. Basic theory, *J. Sci. Comput.* 1 (1) (1986) 3–51.
- [34] B.E. Launder, D.B. Spalding, The numerical computation of turbulent flows, in: Numerical Prediction of Flow, Heat Transfer, Turbulence and Combustion, Elsevier, 1983, pp. 96–116.

- [35] J.F. Williams, D.L. Hawkings, Sound generation by turbulence and surfaces in arbitrary motion, *Philos. Trans. R. Soc. Lond. A* 264 (1151) (1969) 321–342.
- [36] F. Farassat, G.P. Succi, A review of propeller discrete frequency noise prediction technology with emphasis on two current methods for time domain calculations, *J. Sound Vib.* 71 (3) (1980) 399–419.
- [37] D. Casalino, An advanced time approach for acoustic analogy predictions, *J. Sound Vib.* 261 (4) (2003) 583–612.
- [38] D. Casalino, A. Hazir, A. Mann, Turbofan broadband noise prediction using the lattice Boltzmann method, *AIAA J.* 56 (2) (2018) 609–628.
- [39] R.P. Woodward, C.E. Hughes, R.J. Jeracki, C.J. Miller, Fan noise source diagnostic test far-field acoustic results, *AIAA Pap.* 2427 (2002) 2002.
- [40] D. Casalino, F. Avallone, I. Gonzalez-Martino, D. Ragni, Aeroacoustics study of a wavy stator leading edge in a realistic fan/OGV stage, in: *Intl. Symp. on Transport Phenomena and Dynamics of Rotating Machinery*, Maui, HI, 2017.
- [41] J.H. Lienhard, *Synopsis of Lift, Drag, and Vortex Frequency Data for Rigid Circular Cylinders*, vol. 300, Technical Extension Service, Washington State University, 1966.
- [42] D. Casalino, M. Jacob, M. Roger, Prediction of rod-airfoil interaction noise using the Ffowcs-Williams-Hawkings analogy, *AIAA J.* 41 (2) (2003) 182–191.
- [43] D. Lockard, J. Casper, Permeable surface corrections for Ffowcs Williams and Hawkings integrals, in: *11th AIAA/CEAS Aeroacoustics Conference*, 2005, p. 2995.
- [44] I. Gonzalez-Martino, D. Casalino, Fan tonal and broadband noise simulations at transonic operating conditions using lattice-Boltzmann methods, in: *2018 AIAA/CEAS Aeroacoustics Conference*, 2018, p. 3919.
- [45] M.L. Shur, P.R. Spalart, M.K. Strelets, Noise prediction for increasingly complex jets. Part I: methods and tests, *Int. J. Aeroacoust.* 4 (3) (2005) 213–245.
- [46] C. Teruna, D. Casalino, D. Ragni, F. Avallone, Numerical analysis of a linear cascade model for rotor-stator interaction aeroacoustics, in: *2018 AIAA/CEAS Aeroacoustics Conference*, 2018, p. 4189.
- [47] S. Szepessy, P. Bearman, Aspect ratio and end plate effects on vortex shedding from a circular cylinder, *J. Fluid Mech.* 234 (1992) 191–217.
- [48] J. Jeong, F. Hussain, On the identification of a vortex, *J. Fluid Mech.* 285 (1995) 69–94.
- [49] M.S. Howe, *Theory of Vortex Sound*, vol. 33, Cambridge University Press, 2003.
- [50] F. Gea Aguilera, J.R. Gill, D. Angland, X. Zhang, Wavy leading edge airfoils interacting with anisotropic turbulence, in: *23rd AIAA/CEAS Aeroacoustics Conference*, 2017, p. 3370.
- [51] D. Casalino, F. Avallone, I. Gonzalez-Martino, D. Ragni, Aeroacoustic study of a wavy stator leading edge in a realistic fan/OGV stage, *J. Sound Vib.* 442 (2019) 138–154.
- [52] G. Podboy, M. Krupar, S. Helland, C. Hughes, Steady and unsteady flow field measurements within a NASA 22 inch fan model, in: *40th AIAA Aerospace Sciences Meeting & Exhibit*, 2002, p. 1033.
- [53] P. Chaitanya, P. Joseph, S. Narayanan, C. Vanderwel, J. Turner, J.-W. Kim, B. Ganapathisubramani, Performance and mechanism of sinusoidal leading edge serrations for the reduction of turbulence-aerofoil interaction noise, *J. Fluid Mech.* 818 (2017) 435–464.
- [54] J. Boudet, N. Grosjean, M.C. Jacob, Wake-airfoil interaction as broadband noise source: a large-eddy simulation study, *Int. J. Aeroacoust.* 4 (1) (2005) 93–115.
- [55] C. Bogey, C. Bailly, D. Juve, Noise computation using Lighthill's equation with inclusion of mean flow-acoustics interactions, in: *7th AIAA/CEAS Aeroacoustics Conference and Exhibit*, 2001, p. 2255.
- [56] R. Parker, Resonance effects in wake shedding from parallel plates: some experimental observations, *J. Sound Vib.* 4 (1) (1966) 62–72.
- [57] H. Yokoyama, K. Kitamiya, A. Iida, Flows around a cascade of flat plates with acoustic resonance, *Phys. Fluids* 25 (10) (2013) 106104.
- [58] K.A. Kousen, J.M. Verdon, Aeroacoustics of real blade cascades, in: *Unsteady Aerodynamics, Aeroacoustics, and Aeroelasticity of Turbomachines and Propellers*, Springer, 1993, pp. 725–742.
- [59] C. Xu, Y. Mao, Z. Hu, Numerical study of pore-scale flow and noise of an open cell metal foam, *Aerosp. Sci. Technol.* 82 (2018) 185–198.
- [60] L. Garcia-Raffi, L. Salmerón-Contreras, I. Herrero-Durá, R. Picó, J. Redondo, V. Sánchez-Morcillo, K. Staliunas, N. Adkins, A. Cebrecos, N. Jiménez, et al., Broadband reduction of the specular reflections by using sonic crystals: a proof of concept for noise mitigation in aerospace applications, *Aerosp. Sci. Technol.* 73 (2018) 300–308.